nature portfolio

https://doi.org/10.1038/s41563-022-01282-6

Supplementary information

Intrinsic ferroelectricity in Y-doped HfO_2 thin films

In the format provided by the authors and unedited

Supplementary Information

Intrinsic ferroelectricity in Y-doped HfO_2 thin films

Yu Yun,[1†] Pratyush Buragohain,[1†] Ming Li,[1†] Zahra Ahmadi,[2] Yizhi Zhang,[3] Xin Li,[1] Haohan Wang,[1] Jing Li,[1] Ping Lu[4], Lingling Tao,[1] Haiyan Wang,[3] Jeffrey E. Shield,[2,5] Evgeny Y. Tsymbal,[1,5]* Alexei Gruverman,[1,5]* Xiaoshan Xu[1,5]*

[1] Department of Physics and Astronomy, University of Nebraska-Lincoln, Lincoln, Nebraska 68588, USA
[2] Department of Mechanical and Materials Engineering, University of Nebraska–Lincoln, Lincoln, Nebraska 68588, USA
[3] School of Materials Engineering, Purdue University, West Lafayette, Indiana 47907, USA
[4]Sandia National Laboratories, Albuquerque, NM 87185, USA
[5] Nebraska Center for Materials and Nanoscience, University of Nebraska, Lincoln, Nebraska 68588, USA

†Joint first authors.

*Corresponding authors: tsymbal@unl.edu, agruverman2@unl.edu, xiaoshan.xu@unl.edu

Contents

1. Optimization of growth conditions and positive polarization-crystallinity correlation

1.1 Substrate-temperature dependence

YHO (5% Y doped-HfO_2) (111) films were grown on LSMO ($La_{0.7}Sr_{0.3}MnO_3$)/STO ($SrTiO_3$) (001) with various growth temperature (T_s) between 750°C to 970°C. The O_2 background pressure and sample thickness are fixed at 70 mTorr (optimal, see Section 1.2) and ≈ 10 nm (optimal, see Section 1.3), respectively.

The ω-2θ XRD scans of YHO/LSMO/STO (001) films with various T_s are shown in Fig. S1a. Fig. S1b shows the polarization-voltage hysteresis loop (*P-V* loops) of the films grown at different temperature, which indicates that the highest polarization is obtained in films grown at T_s = 890 °C.

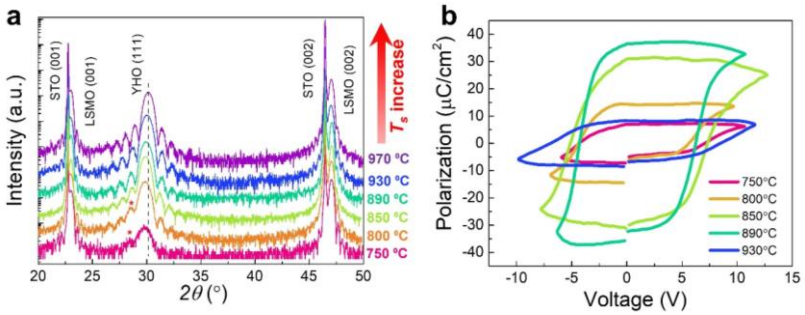

Fig. S1. (a) ω-2θ XRD scans for YHO(111) / LSMO(001) / STO(001) samples with various growth temperature (T_s). The OOP lattice constant of YHO films decreases as the T_s increases. The "*" indicates the $(-111)_m$ of the monoclinic phase. **(b)** *P-V* loops of the YHO/LSMO/STO (001) films grown at various temperature.

The rocking curves of YHO (111) peaks are displayed in Fig. S2. The rocking curve contains two components: a broad peak and a sharp peak, which correspond to parts of the films of low and high crystallinity respectively (see Section 1.4). The sharp/broad peak area ratio can be used to represent the overall crystallinity of the film. Fig. S2 suggests that the crystallinity reaches

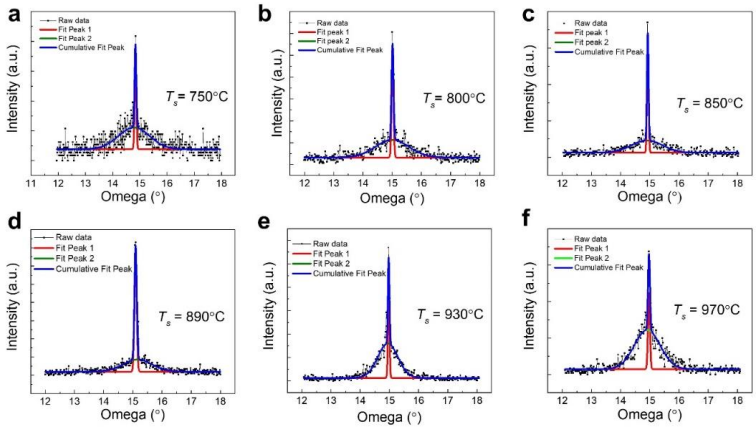

Fig. S2. Rocking curves of the (111) peaks for the YHO(111) films grown on LSMO(001) / STO(001) with various growth temperatures **(a-f)**.

maximum at T_s = 890 °C. The sharp/broad peak area ratio as a function of T_s is shown in Fig. 1e. A clear positive correlation between the crystallinity and the polarization is observed.

The surface morphology of YHO films grown on LSMO/STO (001) was measured by atomic force microscopy (AFM). For $T_s \leq 890$°C, the flat surface with atomic terrace was observed, as depicted in Fig. 2c, and the large/small grain ratio reaches the maximum. As T_s further increases, the surface of the films becomes much rougher and some islands appear around the terraces, as shown in Fig. S3. The areas of the AFM images are 1 μm × 1 μm. The heights of surface along the blue in the AFM images is measured and shown below the AFM images. The heights and sizes of islands increases with T_s, which could be attributed to the decay of LSMO layer due to high growth temperature. These islands could not only reduce the grain size and crystallinity, but also lead to the high leakage current.

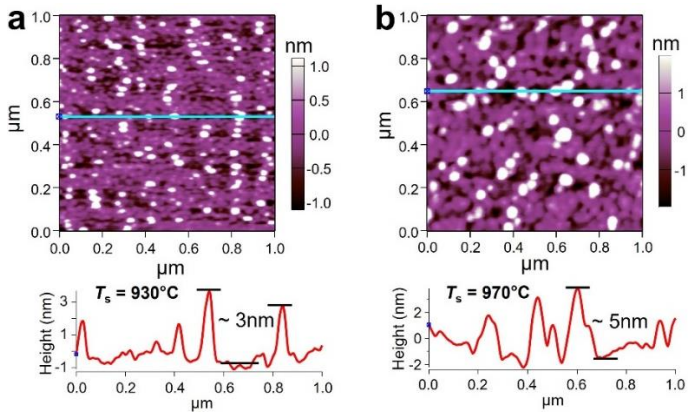

Fig. S3. Atomic force image of YHO(111) / LSMO(001) / STO(001) films with **(a)** T_s = 930°C and **(b)** T_s = 970°C. The height of the islands increases with T_s, which is due to the decay of LSMO layer.

1.2 Background O_2 pressure dependence

The YHO thin films was grown on the LSMO/STO (001) at various oxygen pressure from 1 mTorr to 150 mTorr, as shown in Fig. S4a. The growth temperature and sample thickness are fixed at 890°C and ≈ 10 nm, (see Section 1.1 and 1.3) respectively.

Figure S4b demonstrates that the interplanar spacing $d_{\{111\}}$ decreases as deposition O_2 pressure. To characterize the ferroelectric properties, the *P-V* loops were measured using the PUND method and plotted in Fig. S4c. The coercive voltage increases with deposition O_2 pressure. The polarization reached the maximum value as the deposition O_2 pressure is 70 mTorr.

The rocking curves of YHO (111) peaks are shown in Fig. S4(d-f). For the sample grown under 5 mTorr oxygen pressure (Fig. S4d), the rocking curve only demonstrates a broad peak, indicating a poor crystallinity (see Section 1.4). For the other samples with higher deposition oxygen pressure, the rocking curve could be fitted by two peaks, a sharp peak and a broad peak. Here, the sharp/broaden peak area ratio increase with deposition oxygen pressure initially, then achieve the maximum value as the oxygen pressure is 70 mTorr. As the deposition oxygen pressure further increased, the sharp/broad peak ratio begins to decrease.

The correlation between sharp/broad peak area ratio and polarization is plotted in Fig. S4g, which is consistent with dependence of ferroelectric polarization on temperature.

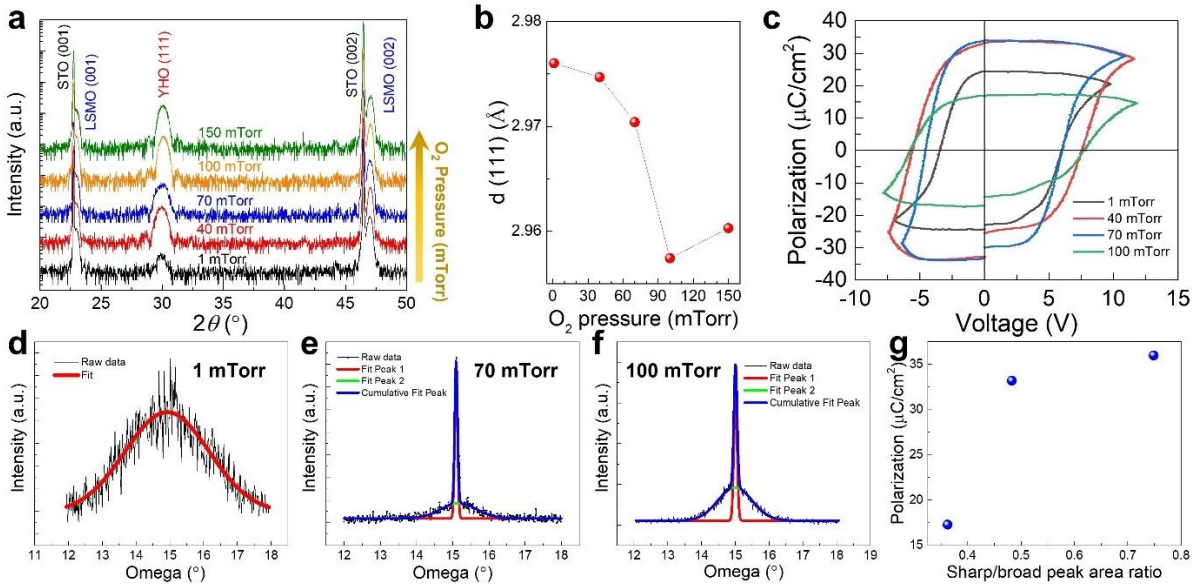

Fig. S4. **(a)** XRD ω-2θ scans of YHO(111) / LSMO(001) / STO(001) films with various deposition oxygen pressure. **(b)** dependence of interplanar spacing $d_{\{111\}}$ on O_2 pressure. **(c)** *P-V* loops for the sample with various deposition oxygen pressure. **(d-f)** Rocking curve of YHO (111) peak for the O_2 pressure series fitted by one or two peaks using Gaussian distribution. **(g)** Polarization as a function of sharp/broaden peak area ratio.

In addition to crystallinity, effect of O_2 growth pressure on local structure have been characterized using the electron microscopy and spectroscopy. As shown in Fig. S5a and b, high-resolution images of transmission electron microscopy (TEM) of the YHO (111)/LSMO (110) films demonstrate higher crystallinity in the film grown in 70 mTorr (optimal) O_2 pressure than that grown in and 150 mTorr O_2 pressure, consistent with the result found from the x-ray diffraction study above.

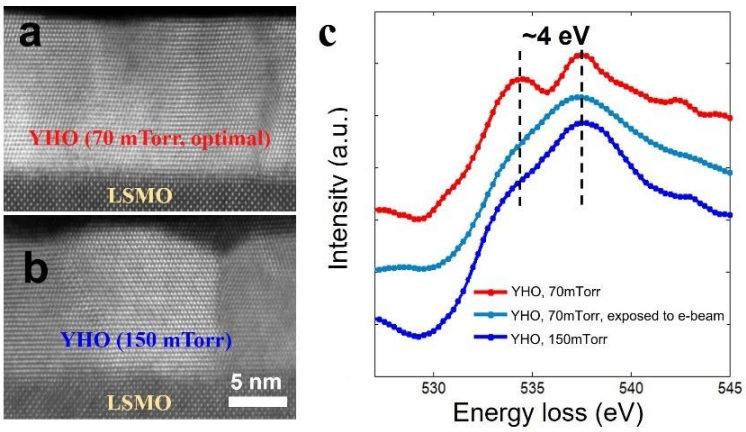

Fig. S5. (a) and **(b)** are the high-resolution scanning transmission electron microscopy (STEM) images of YHO(111) / LSMO(110) / STO(110) films (about 10 nm) grown in 70 mTorr (optimal) and 150 mTorr O_2 pressure respectively. **(c)** Electron energy loss spectroscopy (EELS) the samples in (a) and (b) as well as the sample in (a) exposed to the electron beam at a dose rate of 1.1×10^4 electrons $Å^{-2}$ s^{-1} for ~60 s.

Figure S5c shows the results of the electron energy loss spectroscopy (EELS) measured on the O K edge of the films grown in different O_2 pressure as well as the film grown in the optimal O_2 pressure and exposed to the electron beam. For the film grown in the optimal pressure, two distinct peaks are observed, consistent with the EELS spectra observed previously in well-crystallized HfO_2 and Y doped HfO_2 films [1]. The O K edge absorption corresponds to the electronic excitation from the O 1s states to the O 2p states that are hybridized with the Hf 5d states. The separation between the two peaks is from the crystal field splitting of the Hf 5d states due to the local environment of the surrounding oxygen anions [2]. For the film grown in 150 mTorr O_2 pressure, and that grown in the optimal O_2 pressure and exposed to the electron beam (a dose rate of 1.1×10^4 electrons $Å^{-2}$ s^{-1} for ~60 s), the two peaks are clearly smeared, indicating disorder of local environment of Hf, consistent with the low crystallinity.

1.3 Film thickness dependence

The dependence of thickness of YHO (111)/LSMO (001) films have been systematically investigated, too. The growth temperature and O_2 pressure are fixed at the optimal values 890°C and 70 mTorr, respectively (see Section 1.1 and 1.2).

The thickness of YHO films was measured by x-ray reflectivity (XRR), as shown in Fig. S6. The clear oscillations resulted from the YHO and LSMO layer indicate the smooth interface and surface.

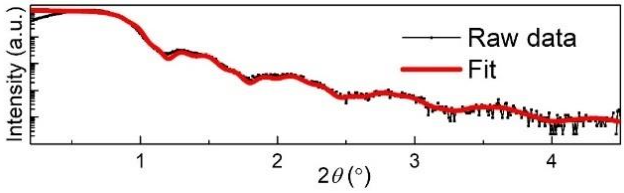

Fig. S6. X-ray reflectivity (XRR) of the YHO(111) / LSMO(001) / STO(001) thin film.

The XRD ω-2θ scans are displayed in Fig. S7a. No obvious impurity phase is observed. As the thickness increases, the width of YHO (111) peaks become smaller and the peak position shifts to high angle. The thickness dependent interplanar spacing $d_{\{111\}}$ is plotted in Fig. S7b. The reduced d-spacing indicates the strain on the sample is relaxing with thickness increase. This strain is not fully relaxed as the YHO thickness is about 10 nm. The structural constraint on the YHO films plays an important role on the ferroelectric phase stabilization and rhombohedral distortion (see Section 3.2).

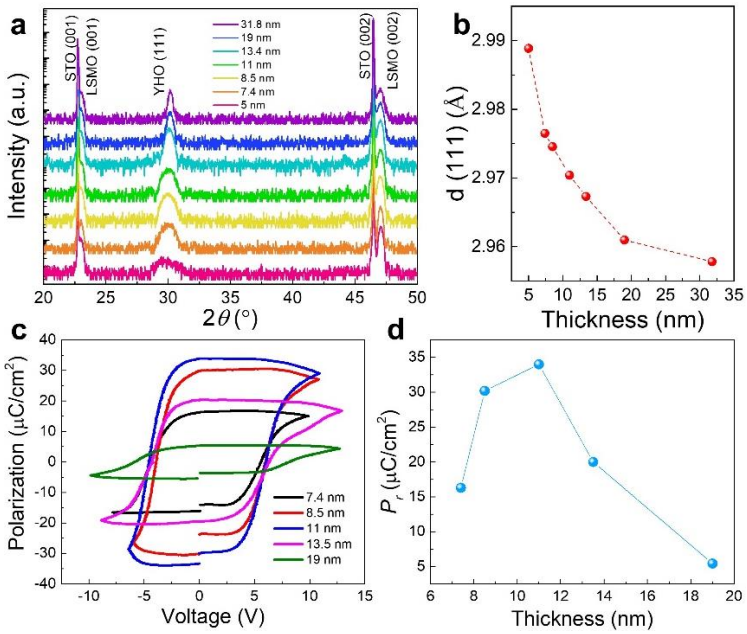

Fig. S7. (a) XRD ω-2θ scans of YHO(111) / LSMO(001) / STO(001) films with various thickness. **(b-d)** dependence of interplanar spacing $d_{\{111\}}$ of YHO films, *P-V* loops, and P_r on thickness.

To characterize the ferroelectric properties, we measured the *P*-*V* loops for the sample with various thicknesses, as shown in Fig. S7c. The thickness dependent polarization is plotted in Fig. S7d. The maximum remanent polarization appears as the thickness is around 10 nm. The trend is consistent with the results in previous literature [3].

1.4 Film crystallinity and size of structural domains

1.4.1 X-ray rocking curve of the out-of-plane *k* points and the film crystallinity

Rocking curves (constant 2θ, scan ω) have been widely used to characterize the crystallinity of epitaxial thin films, where narrower peak width corresponds to higher crystallinity.

As illustrated in Fig. S8a, an OOP rocking curve scans the lateral spread of the reciprocal point, which typically reflects the convoluted effects of the lateral coherence length and the distribution of the crystallite tilt. For the OOP *k* points, the contribution of the tilt to lateral spread increases linearly with the magnitude of *k*, while the contribution of the lateral coherence stays constant. Therefore, by measuring the rocking curve of multiple *k* points along the same direction, more details about the crystallinity of epitaxial thin films can be extracted in terms of tilt and lateral coherence length [4].

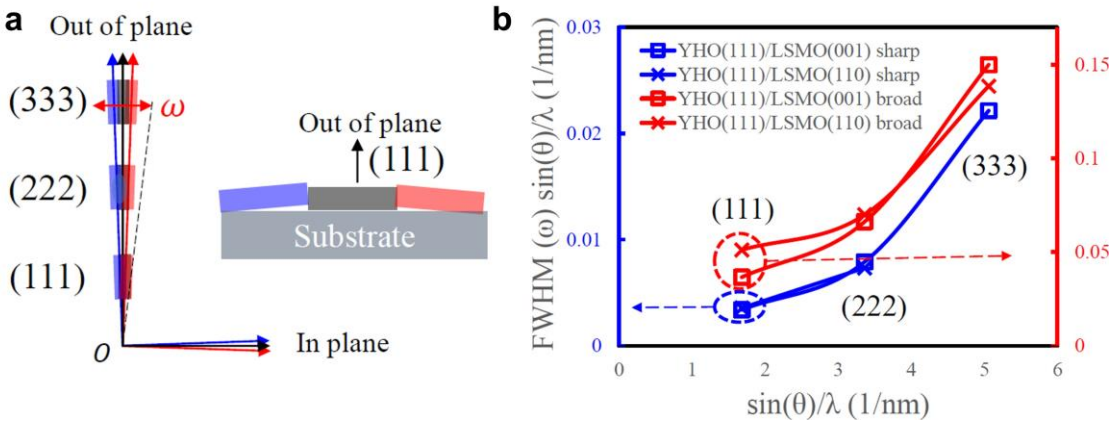

Fig. S8. **(a)** Schematics of the effect of the tilt and lateral coherence length on the spread of the points and the rocking curve width in the reciprocal space. **(b)** William-Hall plot of YHO (111) films grown on LSMO(001) / STO(001) and LSMO(110) / STO(110) for the (111), (222), and (333) rocking curves. The lines are guides to the eyes.

Here we carried out the William-Hall analysis [4] on the rocking curves of multiple *k* points, i.e., (111), (222), and (333) for both the YHO(111)/LSMO(001) and the YHO(111)/LSMO(001) films grown at the optimal condition. As shown in Fig. S8b, FWHM(ω) sin(θ)/λ (proportional to the lateral spread of *k*) is plotted against sin(θ)/λ (proportional to the magnitude of *k*) for both the sharp and broad peaks.

For both the sharp and the broad peaks (see Fig. S2 for the example of rocking curves consisting of a sharp peak sitting on a broad peak), the lateral spread of *k* significantly increases with the magnitude of *k*, indicating that a large contribution from the distribution of the tilt angle of the crystallites, ~ 0.1º and ~ 1º degree FWHM for the sharp and broad peaks respectively. On the other hand, the lateral spread of *k* appears to approach a finite intercept when *k* approaches zero, indicating a finite lateral coherence length. If we use the value for (111) as the upper limit of the intercept, the lower limit of the lateral coherence length can be estimated as ~10 nm and ~100 nm for the sharp and broad peaks respectively. The large lateral coherence length is consistent with the observation of continuous YHO (111) planes over a long lateral scale in Fig. S9.

The feature of a sharp peak sitting on a broad background in rocking curves has been often observed in epitaxial thin films, indicating two parts of the films with different crystallinity.[5,6] The relative intensity of the two peaks represents the relative population of the two parts. In case of the YHO (111) films studied in this work, the sharp (broad) peak in the rocking curve represents a part of the film of higher (lower) crystallinity in terms of smaller (larger) tilt and longer (shorter) lateral coherence length. Hence, we use the ratio between the areas of the sharp and broad peaks (sharp/broad peak area ratio) as a parameter to represent the crystallinity.

1.4.2 Transmission electron microscopy

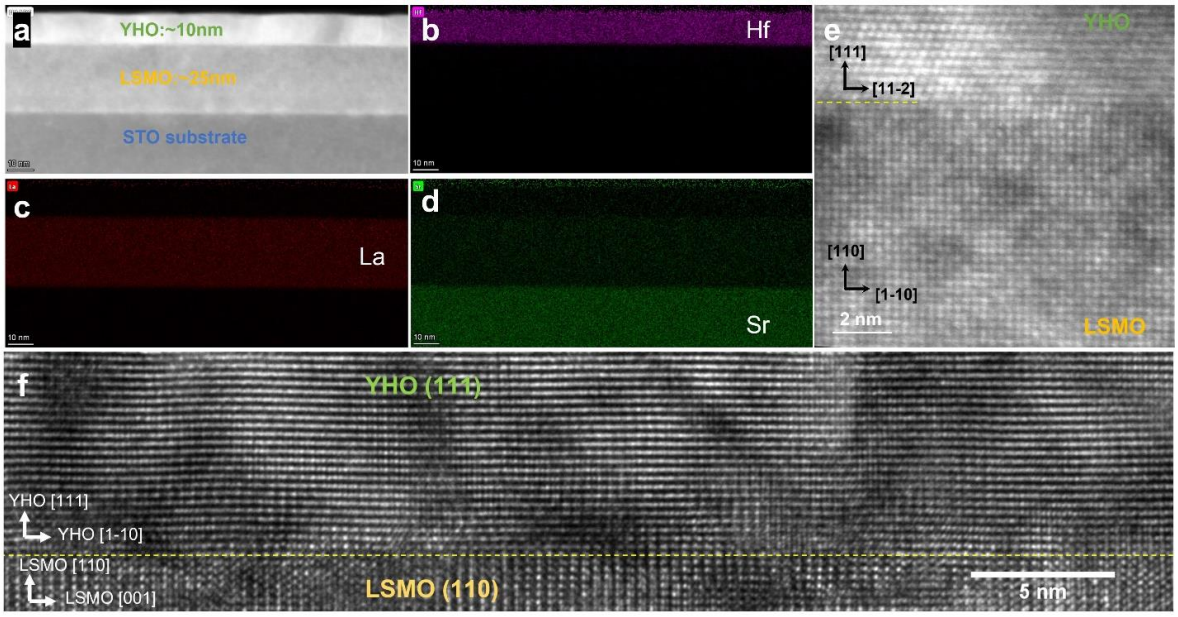

Fig. S9. (S)TEM image of YHO(111) / LSMO(110) / STO(110) films. **(a)** Low magnification STEM-HAADF image of the YHO/LSMO/STO (110) stack. **(b-d)** EDS mapping of Hf, La, and Sr respectively of the same area as (a). **(e,f)** shows the epitaxial relation YHO [$11\bar{2}$] // LSMO [$1\bar{1}0$] and YHO [$1\bar{1}0$]// LSMO [001].

To further investigate the crystal structure of YHO/LSMO/STO (110) films, we carried out the scanning transmission electron microscopy (STEM) analysis. The low magnification STEM image of YHO (111)/LSMO (110) films taken under the high angle annular dark field (HAADF) mode is shown in Fig. S9a. The different layers are labeled. The energy dispersive x-ray spectroscopy (EDS) mapping demonstrates the element distribution of Hf, La and Sr (Fig. S9b, c and d). Fig. S9e and f show the interface between the YHO film and the LSMO bottom electrode with clear interface between the layers. The epitaxial relationships are determined to be YHO [$11\bar{2}$] // LSMO [$1\bar{1}0$] and YHO [$1\bar{1}0$]// LSMO [001]. The entire TEM image (Fig. S9f) appears to consist of continuous YHO (111) layers. This is consistent with the large lateral correlation of the films measured by the x-ray diffraction rocking curve, because the lateral coherence length measured using a symmetric rocking curve on an OOP *k*-point, such as (111) for the (111) oriented film, is most sensitive to the flatness of the crystal planes that are parallel to the film surface [7].

1.4.3 Lateral size of the structural domain and profile of the crystallites

For the YHO (111) films grown on LSMO (001) and LSMO (110), there are 4 and 2 types of structural domains respectively within the (111) planes (see Section 3), due to the mismatched film and substrate rotational symmetry. The lateral size of the domains can be much smaller than that of the lateral coherence length found using the rocking curve measurements.

The profile of crystallites can be found by scanning the reciprocal space points using the ω-2θ scan. As illustrated in Fig. 10a and b, the profile of the reciprocal points reflects the profile of the crystallites as $\Delta k = \frac{2\pi}{\Delta r}$, where Δk can be found from the ω-2θ scan as $\Delta k = \frac{2\pi}{\lambda} 2\cos\theta\, \Delta\theta$. If $w_{2\theta} \propto \Delta\theta$ is the full-width-high-maximum of the ω-2θ scan peak, this leads to the famous Sherrer formula: $\Delta r = \frac{0.9\lambda}{\cos\theta w_{2\theta}}$. In the epitaxial thin films, assuming χ is the angle between $\vec{k}$ and $\hat{z}$ (OOP direction), by scanning $\vec{k}$ points of different χ and measure $w_{2\theta}$, one can draw the profile of both the *k* space points and the crystallites in real space.

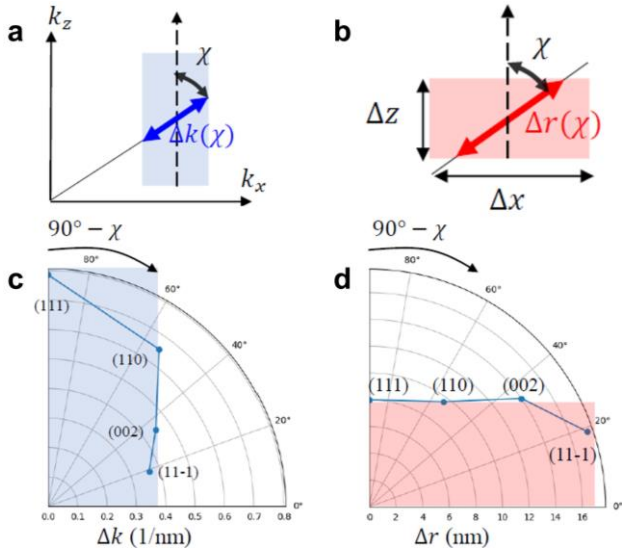

Fig. S10. **(a)** and **(b)** are schematic illustration of the measurement of crystallite profiles using the ω-2θ scan. **(c)** and **(d)** are the results from the ω-2θ scan of (111), (110), (002), and (11-1) points of a YHO (111) / LSMO(110) / STO(110) film grown at the optimal growth condition.

Figure S10c and d are the results of scanning the (111), (110), (002), and (11-1) peaks of a YHO (111)/LSMO (110) films grown at the optimal condition. Note that for the (111)-oriented films, (111) is the OOP reciprocal point, for which the Δr value is the film thickness that can be verified using x-ray reflectivity. According to the data, the lateral size of the crystallites is about 17 nm. Notice in this work, the crystallites correspond to the domains of the YHO (111) with different in-plane orientation.

2. Intrinsic ferroelectricity

2.1 Frozen imprint behavior at low temperature

Temperature-dependent imprint behavior was characterized as shown in Fig. S11. Previously, it was shown that the direction of imprint was strongly dependent on the poling history – if the last poling pulse was positive (negative), then the imprint or the internal bias will be negative (positive). This tunable imprint is called fluid imprint, which could be attributed to charge injection and subsequent trapping at defect sites at the interface between YHO films and electrodes [8]. In addition, the magnitude of the imprint was found to gradually increase with time [3]. At room temperature, such a fluid imprint behavior was observed on the capacitors with YHO films grown on LSMO/STO (110) (Fig. S11), where the *P*-*V* loops were found to be left or right shifted depending on whether the polarity of the last pulse was positive or negative. However, at 20 K, the imprint remains 'frozen-in' (Fig. S11b and c) and the direction of the imprint was found to be only dependent on the polarity of the last pulse that was applied to the capacitors before cooling down from room temperature. The imprint did not change even after waiting for nearly 2 hours after reversing the polarity of the poling pulses. This suggests that there is minimal movement of additional charges such as oxygen vacancies at 20 K, which can otherwise move under the depolarization field at higher temperatures. The contribution of the oxygen migration on the polarization switching, which was identified as the main source of large polarization of the HZO epitaxial films at room temperature [9], could thus be excluded.

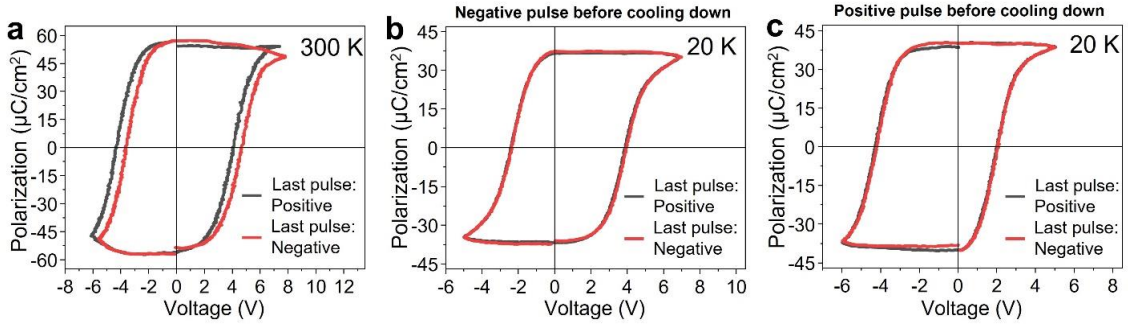

Fig. S11. Imprint at different temperatures for YHO(111) / LSMO(110) / STO(110) films grown at the optimal condition. **(a)** *P*-*V* loops at 300 K after the positive and negative set pulse. The imprint depends on the previous pulse. Imprint at 20 K with **(b)** negative set pulse and **(c)** positive set pulse before cooling down. The imprint cannot be changed by the set pulse at 20K, indicating that oxygen migration is restricted strongly.

2.2 Long endurance at low temperature

The endurance of the devices with YHO films grown on LSMO/STO (110) was measured, as shown in Fig. S12. A triangular pulse pattern was used to cycle the capacitor between the opposite polarization states. The amplitude of the triangular pulse pattern was +/- 5.5 V which was sufficient to switch the polarization at 20 K. The frequency of the triangular pulse was 10 kHz.

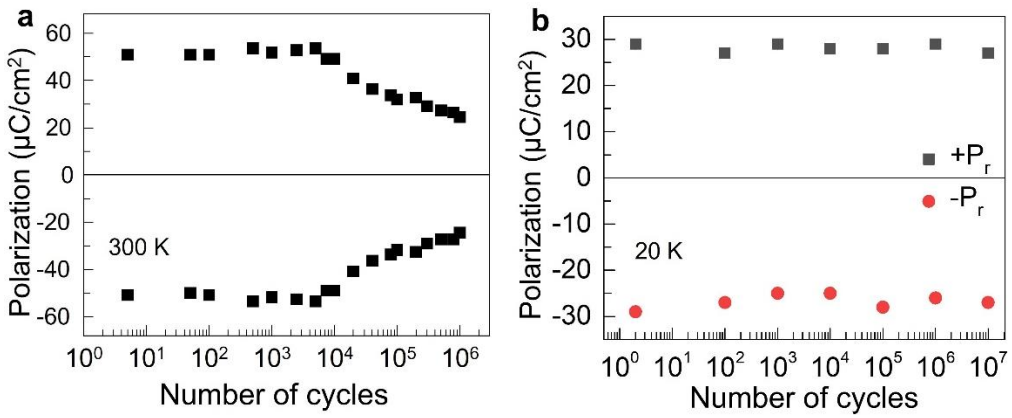

Fig. S12. The endurance of YHO(111) / LSMO(110) / STO(110) films measured at 300 K **(a)** and 20 K **(b)**. YHO thin films were grown at the optimal condition.

For the room-temperature measurement (Fig. S12a), the polarization was almost constant (~ 50 μC/cm^2) until about 10^4 cycles. As the number of cycles further increases, polarization starts to decrease gradually. This instabilities in the field cycling process are commonly observed and explained by the defect (i.e., oxygen vacancies) movement and generation[10]. The endurance measurements at 20 K (Fig. S12b) demonstrated that no reduction in polarization was observed, up to 10^7 cycles. This also highlights that the instabilities induced by the defect movement or oxygen migration could be strongly restricted at low temperature.

2.3 μs switching time scale

In addition, the time scale of the switching process as a function of applied voltage at 300 K was measured as shown in Fig. S13. The typical switching time (t_{SW}) is from 12 μs to 26 μs, which is must faster than the results in HZO films previously [9] and consistent with the timescale of other ferroelectric oxides such as PZT ($Pb(Zr_{0.4}Ti_{0.6})O_3$, $Pb(Zr_{0.2}Ti_{0.8})O_3$) [11,12] and $BiFeO_3$.[13]

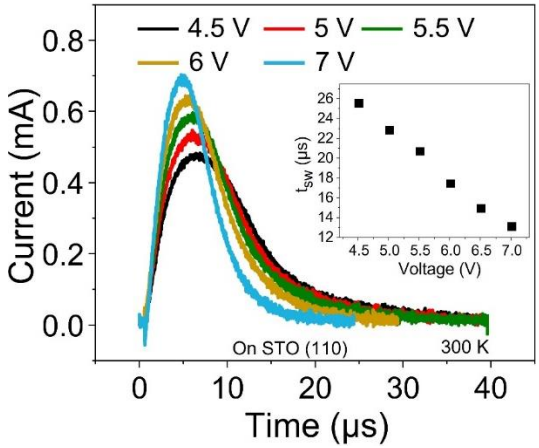

Fig. S13. Switching time with various applied voltage at 300 K of YHO(111) / LSMO(110) / STO(110) films grown at optimal condition.

3 Orthorhombic ($Pca2_1$) structure of YHO with rhombohedral distortion

3.1 Orthorhombic ($Pca2_1$) structure

To quantify the orthorhombic distortion, we carried out the measurements of {002} d-spacing, which is sensitive to the difference of lattice constant *a*, *b*, *c*. The derivation of angle α, β, γ from 90° is quite small, which can only give a secondary contribution to lattice constant. The representative measurements of {002} d spacing of YHO films grown on LSMO/STO (001) and LSMO/STO (110) at χ = 55° are plotted in Fig. S14a and b, respectively.

The {002} peaks can be fitted very well by double gaussian peaks, as shown in Fig. S15. The double peaks correspond to the two different lattice constants, which is important evidence of the orthorhombic distortion, as we mentioned in main text.

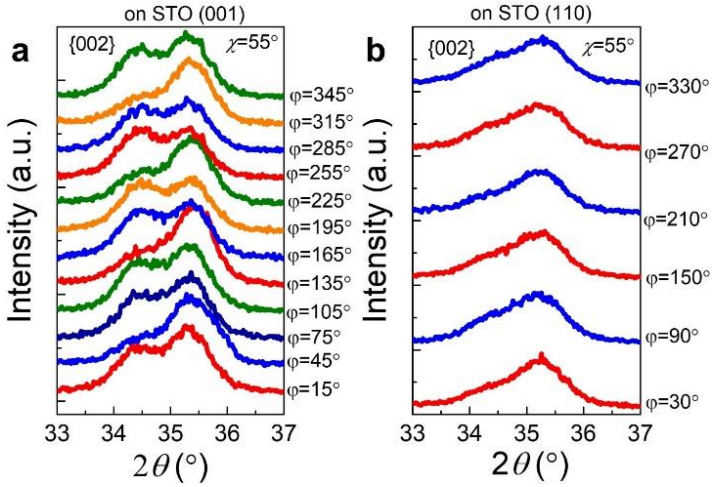

Fig. S14. The 2θ scan of the {002} peaks for YHO films grown on **(a)** LSMO(001) / STO(001) and **(b)** LSMO(110) / STO(110) grown at the optimal condition.

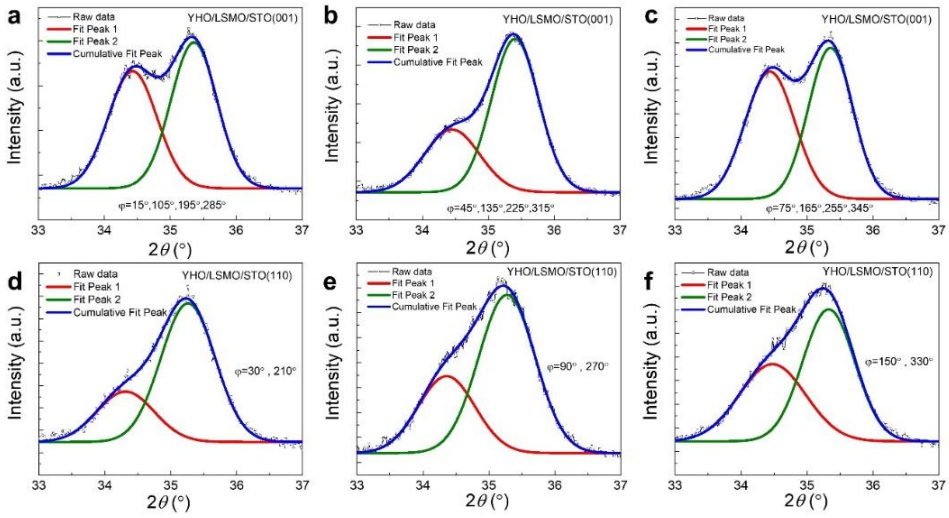

Fig. S15. The fitting of {002} peaks of YHO films grown on **(a-c)** LSMO(001) / STO(001) and **(d-f)** LSMO(110) /STO(110) with various φ angle.

The reflection high energy electron diffraction (RHEED) patterns of the YHO/LSMO/STO (110) films at room temperature are shown in Fig. S16. The clear streaks for each layers suggest the good crystallinity and smooth surface and interface. The epitaxial relationship is consistent with the results of TEM in Fig. S9.

The observation of the {110} diffraction using RHEED as well as the observation of the (001) and (110) peaks in the main text [Fig. 4(d, e)] indicate the $Pca2_1$ ferroelectric orthorhombic structure.

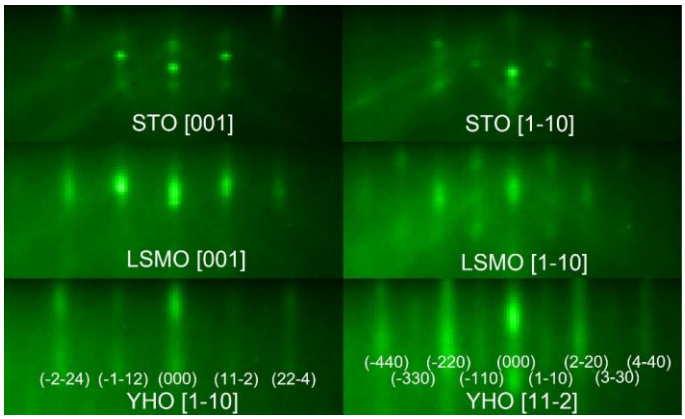

Fig. S16. The RHEED pattern of each layer of YHO(111) / LSMO(110) / STO(110) films. The e-beams are parallel to STO [001] (left column) and STO [1-10] (right column), respectively.

3.2 Rhombohedral distortion

3.2.1 YHO (111)/LSMO (001)/STO (001) films

The rhombohedral distortion of the YHO (111)/LSMO (001) films is characterized by the measurements of {111} d-spacing using the Bruker D8 XRD with 2D detector. The measurement of {111} d spacing is sensitive to the rhombohedral distortion. The difference in lattice parameter in *a*, *b*, *c* only can give a second order contribution. The 2θ scans of {111} peaks along OOP and IP direction with χ = 71° for the samples with optimal growth condition are displayed in Fig. S17a. The IP {111} peaks with various φ angle are at the similar 2θ angle, which is distinctly higher than the 2θ angle of OOP {111} peaks. This is the signature of the rhombohedral symmetry [14,15]. The 12-fold IP symmetry resulted from the symmetry mismatch between YHO and LSMO films [14,15]. The corresponding {111} d-spacing values are summarized in Fig. S17b.

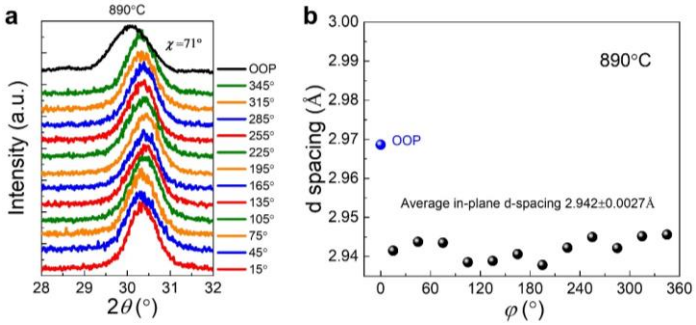

Fig. S17. The 2θ scans of {111} peaks **(a)** and {111} d-spacing **(b)** along OOP and IP with φ angle differing by 30° at an angle (χ) of ~71° for the YHO (111) / LSMO (001) / STO (001) films grown at the optimal growth condition.

The OOP d-spacing decreases with T_s. Meanwhile, IP d-spacing keeps almost constant, as shown in Fig. S18. This suggests that the anisotropy of strain and stress reduced as T_s increases. The trend of OOP d-spacing is consistent with the previous reports about HZO films [3]. Regarding the nonlinear trend of the polarization as a function of the T_s in Fig. 1e, the strain effect is unlikely the reason of the evolution of the polarization with various T_s.

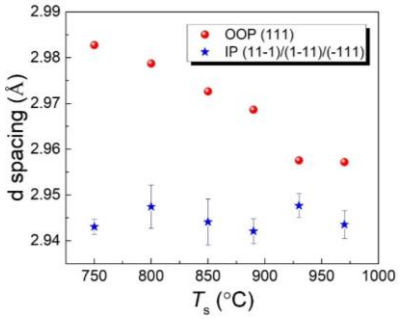

Fig. S18. The d-spacing of OOP (111) and average IP d-spacing (11-1)/(1-11)/(-111) as a function of growth temperature (T_s) for the YHO (111) / LSMO (001) / STO(001) films.

3.2.2 YHO (111)/LSMO (110)/STO (110) films

The rhombohedral distortion in YHO (111) films grown on LSMO (110)/STO (110) is also evident in Fig. S19. There is also a distinct difference between OOP and IP d-spacing, indicating the rhombohedral distortion also exists. The rhombohedral distortion of YHO (111)/LSMO (110) is smaller than that of YHO (111)/LSMO (001), as displayed in Table 1. The YHO (111) films grown on LSMO (110)/STO (110) exhibits 6-fold symmetry with 2 different domains rotated by 180°, which is attributed to the 2-fold symmetry of the substrate and 3-fold symmetry of the YHO films. This heterostructure could give rise to the reduced grain boundary and better crystallinity. The epitaxial relationship and XRD aliment are illustrated in the inset of Fig. S19b.

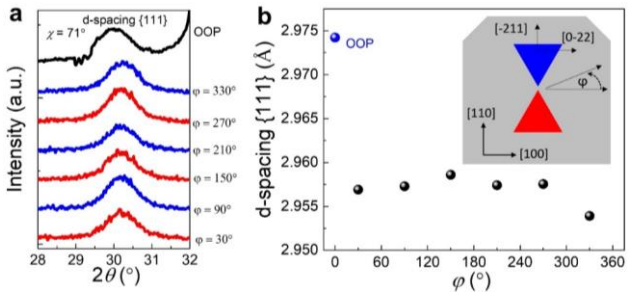

Fig. S19. The d-spacing {111} of the YHO(111) / LSMO(110) /STO(110) films grown at the optimal condition. **(a)** The 2θ scan of {111} peaks along OOP and IP direction. **(b)** The {111} d spacing. Inset: epitaxial relationship between YHO and LSMO/STO (110), and the azimuthal direction represents φ, with a (0°–360°) range.

3.3 Density functional theory studies

To explore the effects of the rhombohedral distortion on the structural stability and ferroelectric polarization of the Y-doped HfO_2, we performed density-functional theory (DFT) calculations as described in Methods. We started from the orthorhombic $Pca2_1$ unit cell of undoped HfO_2 where the interaxial angles were $\alpha = \beta = \gamma = 90°$ (Fig. S20a). Then, we introduced a small rhombohedral distortion by reducing the angles while keeping them equal, i.e., $\alpha = \beta = \gamma < 90°$. Throughout the calculations, the experimental values of the lattice parameters were assumed and fixed to be $a = c = 5.07$ Å and $b = 5.20$ Å, and only inner atomic positions were relaxed. Similar calculations were also performed for the 5% Y-doped HfO_2, where effects of doping were modelled by the Virtual Crystal Approximation (see Methods for details).

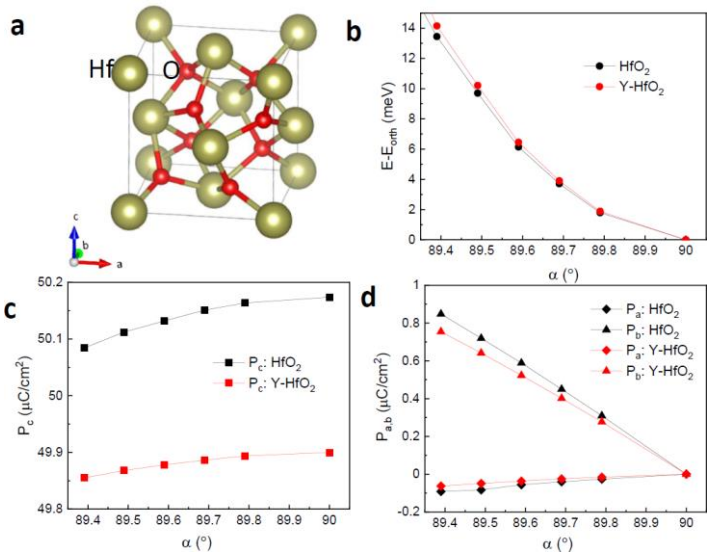

Fig. S20. Results of DFT calculations for bulk undoped and 5% Y-doped HfO_2. **(a)** The atomic structure of an orthorhombic HfO_2 unit cell used in the DFT calculations. **(b)** Change in the total energy of bulk undoped HfO_2 (black lines and symbols) and 5% Y-doped HfO_2 (red lines and symbols) as a function of rhombohedral distortion of the orthorhombic $Pca2_1$ unit cell quantified by angle α. The energy of the orthorhombic $Pca2_1$ structure ($\alpha = 90°$) E_{orth} is taken as a reference. **(c, d)** Calculated components of ferroelectric polarization (c) along the *c*-axis (squares) and (d) along the *a*- (diamonds) and *b*- (triangles) axes as a function of angle α for bulk undoped HfO_2 (black lines and symbols) and 5% Y-doped HfO_2 (red lines and symbols).

We found that rhombohedral distortion of the orthorhombic phase enhances the total energy of both the undoped and Y-doped HfO_2. As seen from Fig. S20b, the total energy is increased by about 6 meV per unit cell with the angle α being reduced from 90° to 89.6° corresponding to our XRD data. This result indicates that the rhombohedral distortion occurring in our experiment is does not minimize the bulk total energy of the grown hafnia film but rather is a consequence of the strain imposed by the substrate.

The calculated ferroelectric polarization of the orthorhombic $Pca2_1$ phase of HfO_2 is about 50.2 $\mu C/cm^2$, which is consistent with the previous theoretical studies. The polarization is directed along the *c*-axis, as enforced by the symmetry of the crystal, so that the *a*- and *b*- components of polarization are zero. The 5% Y doping slightly reduces the polarization down to about 49.9 $\mu C/cm^2$, which indicates that Y does not play a decisive intrinsic role in high polarization values observed in our experiments, but rather helps to stabilize the orthorhombic $Pca2_1$ phase of hafnia.

Fig. S20c shows the calculated *c*-component of the ferroelectric polarization P_c as a function of angle α. With a larger rhombohedral distortion (smaller α), the P_c remains large, but slightly reduces. This reduction is just ~0.1 μC/cm^2 for the degree of distortion relevant to our experiment. At the same time the broken $Pca2_1$ symmetry allows the appearance of non-vanishing *a*- and *b*- components of polarization, P_a and P_b. Fig. S20d shows that the absolute values of both P_a and P_b increase with decreasing α, but the magnitudes are much smaller than P_c. Y-doped HfO_2 exhibits the same tendency as the pristine HfO_2 (compare the red land black lines in Fig. S20c, d), implying an idle role of the doping in the polarization enhancement.

Overall, we conclude from our DFT calculations that the rhombohedral distortion observed in our experiments is not intrinsic to the bulk HfO_2 and most likely results from the strain imposed by the substrate. On the other hand, the rhombohedral distortion of the degree observed in our experiments does not much harm the large ferroelectric polarization value of the orthorhombic $Pca2_1$ phase of the pristine and Y-doped hafnia.

3.4 In-plane polarization

Since in the orthorhombic structure the polarization is along the *c* axis, in addition to the out of plane (OOP) direction, the polarization is expected to also have significant projection in the in-plane (IP) direction of the YHO (111) films, which is verified below.

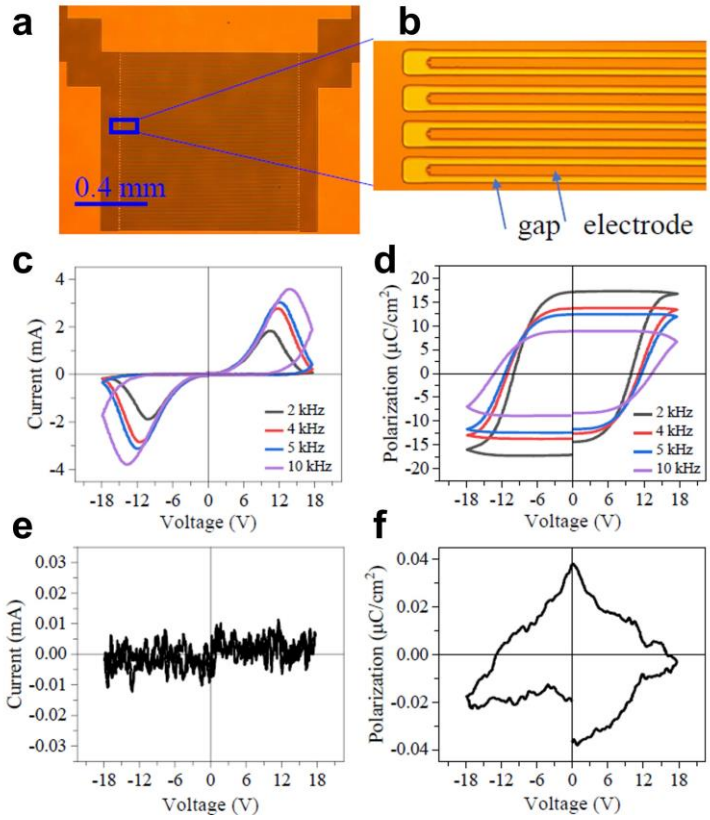

Fig. S21. **(a)** and **(b)** are the optical microscope image of the IP inter-digitized electrodes pattern on YHO (111) (8.3 nm)/ LSMO (110) (3 nm)/STO (110). The gaps between the electrodes are 4 μm wide. **(c)** and **(d)** are the current and polarization as a function voltage measured using the IP electrodes. **(e)** and **(f)** are the current and voltage measured using one top Pt electrode and the LSMO layer as the bottom electrode.

We have studied the IP polarization using a YHO (111) (8.3 nm) film grown on LSMO (3 nm)/STO (110). In order to minimize the contribution of OOP polarization to the measurements, we have reduced the LSMO layer to 3 nm (resistance ~ 1 MΩ), compared with the 25 nm LSMO (~ 1 kΩ) layer in other samples studied in this work.

As shown in Fig. S21a and b, IP inter-digitized Pt electrodes have been patterned on the YHO film using photolithography with 4 μm gaps. Fig. S21c and d are measured using the in-plane electrodes. The polarization is calculated using the switching current and the area of the electrode. We note that the polarization is underestimated due to the geometry of the measurement. Clear switching current and polarization-voltage hysteresis have been observed. Saturated in-plane remanent polarization (P_r) of ≈ 17 μC/cm^2 was observed, which is comparable to the OOP remanent polarization (≈ 50 μC/cm^2) measured in YHO (111) /LSMO (110) films.

To verify that there was no OOP polarization component, we applied the bias to one of the in-plane electrodes and collected the current through the bottom electrode. No measurable

switching current and polarization were observed in this geometry due to the high resistance of the LSMO layer, as shown in Fig. S21e and f.

References

1 Wang, X. F., Li, Q. & Moreno, M. S. Effect of Al and Y incorporation on the structure of HfO_2. *J. Appl. Phys.* **104**, 093529 (2008).

2 Vlachos, D., Craven, A. J. & McComb, D. The influence of dopant concentration on the oxygen K-edge ELNES and XANES in yttriastabilized zirconia. *J. Phys. Condens. Matter* **13**, 10799-10809 (2001).

3 Lyu, J., Fina, I., Solanas, R., Fontcuberta, J. & Sanchez, F. Growth Window of Ferroelectric Epitaxial $Hf_{0.5}Zr_{0.5}O_2$ Thin Films. *ACS Appl. Electron. Mater.* **1**, 220-228 (2019).

4 Chierchia, R. *et al.* Microstructure of heteroepitaxial GaN revealed by x-ray diffraction. *J. Appl. Phys.* **93**, 8918-8925 (2003).

5 Lee, H. G. *et al.* Double-layer buffer template to grow commensurate epitaxial $BaBiO_3$ thin films. *APL Mater.* **4**, 126106 (2016).

6 Marcaud, G. *et al.* High-quality crystalline yttria-stabilized-zirconia thin layer for photonic applications. *Phys. Rev. Mater.* **2**, 035202 (2018).

7 Heying, B. *et al.* Role of threading dislocation structure on the x-ray diffraction peak widths in epitaxial GaN films. *Appl. Phys. Lett.* **68**, 643-645 (1996).

8 Buragohain, P. *et al.* Fluid Imprint and Inertial Switching in Ferroelectric La:HfO_2 Capacitors. *ACS Appl. Mater. Interfaces* **11**, 35115-35121 (2019).

9 Nukala, P. *et al.* Reversible oxygen migration and phase transitions in hafnia-based ferroelectric devices. *Science* **372**, 630-635 (2021).

10 Islamov, D. R. *et al.* Identification of the nature of traps involved in the field cycling of $Hf_{0.5}Zr_{0.5}O_2$-based ferroelectric thin films. *Acta Mater.* **166**, 47-55 (2019).

11 Y. W. So, D. J. Kim, Noh, T. W., Yoon, J.-G. & Song, T. K. Polarization switching kinetics of epitaxial $Pb(Zr_{0.4}Ti_{0.6})O_3$ thin films. *Appl. Phys. Lett.* **86**, 092905 (2005).

12 Lia, W. & Alexe, M. Investigation on switching kinetics in epitaxial $Pb(Zr_{0.2}Ti_{0.8})O_3$ ferroelectric thin films: Role of the 90° domain walls. *Appl. Phys. Lett.* **91**, 262903 (2007).

13 Daniel Pantel *et al.* Switching kinetics in $BiFeO_3$ epitaxial films. *J. Appl. Phys.* **107**, 084111 (2010).

14 Wei, Y. F. *et al.* A rhombohedral ferroelectric phase in epitaxially strained $Hf_{0.5}Zr_{0.5}O_2$ thin films. *Nat. Mater.* **17**, 1095-1100 (2018).

15 Nukala, P. *et al.* Guidelines for the stabilization of a polar rhombohedral phase in epitaxial $Hf_{0.5}Zr_{0.5}O_2$ thin films. *Ferroelectrics* **569**, 148-163 (2020).